Journal of Power Sources 196 (2011) 3223–3232

Contents lists available at ScienceDirect

Journal of Power Sources

journal homepage: www.elsevier.com/locate/jpowsour

An analytical model of view factors for radiation heat transfer in planar and tubular solid oxide fuel cells

Cheng Bao[a,b,*], Ningsheng Cai[b], Eric Croiset[b,c]

[a] Department of Thermal Science and Energy Engineering, School of Mechanical Engineering, University of Science & Technology Beijing, Beijing 100083, PR China
[b] Key Laboratory for Thermal Science and Power Engineering of Ministry of Education, Tsinghua University, Beijing 100084, PR China
[c] Department of Chemical Engineering, University of Waterloo, Waterloo, Ontario N2L 3G1, Canada

ARTICLE INFO

Article history:
Received 10 November 2010
Accepted 12 November 2010
Available online 27 November 2010

Keywords:
Analytical view factor
Differential
Finite-difference
Solid oxide fuel cell
Radiation

ABSTRACT

Radiant heat transfer plays an important role in the distribution of cell temperature and current density in solid oxide fuel cells (SOFC). The objective of this paper is to introduce a mathematical model of view factors for radiation heat exchange in an in-house longitudinally distributed SOFC model. A differential view factor model is first developed for planar and tubular SOFC configurations, but is found invalid when the infinitesimal element size is comparable to the characteristic size. Then, a finite-difference view factor model is developed to solve the problem of discontinuities in the differential view factor model. Starting from a classical problem of convective and radiant heat transfer for a transparent gas flow in a gray-wall tube, a fast and accurate computation is available for the finite-difference view factor model without extra mathematical derivations of the governing equations. Compared to the simple modeling which only takes into account the surface-to-surface radiation exchange between two directly opposed elements, the detailed radiation model based on analytical view factors predicts more uniform distribution of cell temperature and current density in the overall SOFC modeling.

1. Introduction

Solid oxide fuel cells (SOFCs) are a type of high-temperature fuel cells. Planar and tubular configurations are the two most common SOFC designs. With the advantages of short current path and lower component fabrication cost, the planar design is usually the preferred design, but it suffers from sealing problems caused by thermal expansion at high-temperature. Until now, planar design has been widely used in anode-supported intermediate temperature SOFCs [1]. The tubular design is superior with respect to sealing, but often has to operate in the high temperature range of 900–1000 °C to maintain acceptable ohmic polarization due to long current paths. Some other advanced configurations, such as the Siemens Westinghouse design of flattened tubular SOFC and the integrated planar SOFC pioneered by Rolls–Royce (which combines the advantages of the planar and tubular designs by introducing the multi-cell membrane electrode assembly (MEA) concept [2]) can be considered as a variation of the two basic planar and tubular designs [1].

Radiation heat transfer plays an important role in the distribution of cell temperature and current density in SOFCs. A SOFC model with detailed radiation model is necessary for accurate prediction of cell performance. A spectral radiative heat transfer analysis within a computational fluid dynamics (CFD) SOFC model is powerful but usually computationally expensive [3]. A simple method of modeling the surface-to-surface radiation exchange is generally acceptable in thermal models of SOFCs. However, most of state-of-the-art radiation models just considered the radiation exchange between two directly opposed differential elements, where the view factor between the two finite elements is considered identical to that between two infinite diffuse interchange surfaces [4–6]. Some other papers includes radiation exchange among three adjacent control volumes, but the constant view factors are strongly dependent on the number of discrete grids [7,8]. Aiming at system-level analysis, an in-house multi-level simulation platform for solid oxide fuel cell and gas turbine hybrid generation system was recently developed in gPROMS, a commercial advanced process modeling software [9]. The objective of this paper is to introduce an analytical model of view factors in our longitudinally distributed models of planar and tubular SOFCs [10].

Fig. 1 shows the schematic diagram of a section of planar and tubular SOFCs. For planar SOFCs (PSOFC), W_{ch} and D_{ch} are the width and depth of the rectangular flow channel enclosed between the positive electrolyte negative (PEN) and the interconnect (CON). The geometry of tubular SOFCs (TSOFC) is that of the commercial West-

* Corresponding author at: Department of Thermal Science and Energy Engineering, School of Mechanical Engineering, University of Science & Technology Beijing, Beijing 100083, PR China. Tel.: +86 10 62333682; fax: +86 10 62329145.
E-mail address: baocheng@mail.tsinghua.edu.cn (C. Bao).

0378-7753/$ – see front matter © 2010 Elsevier B.V. All rights reserved.
doi:10.1016/j.jpowsour.2010.11.128

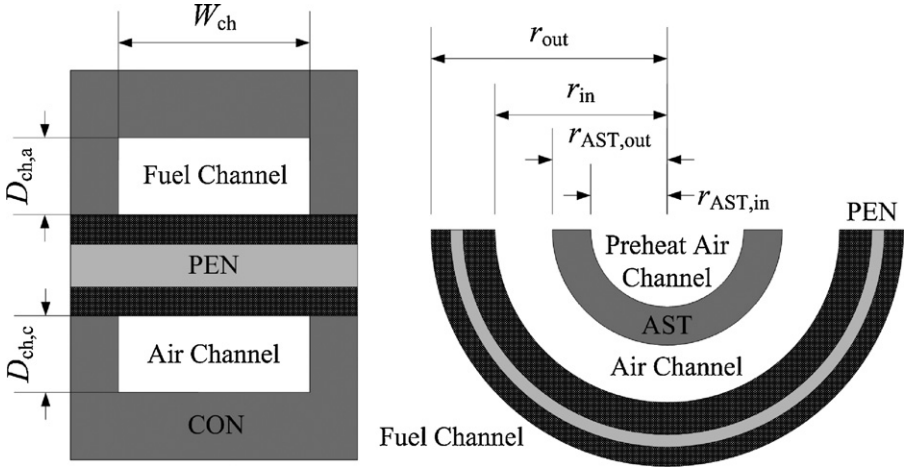

Fig. 1. Schematic diagram of a section of planar and tubular SOFCs.

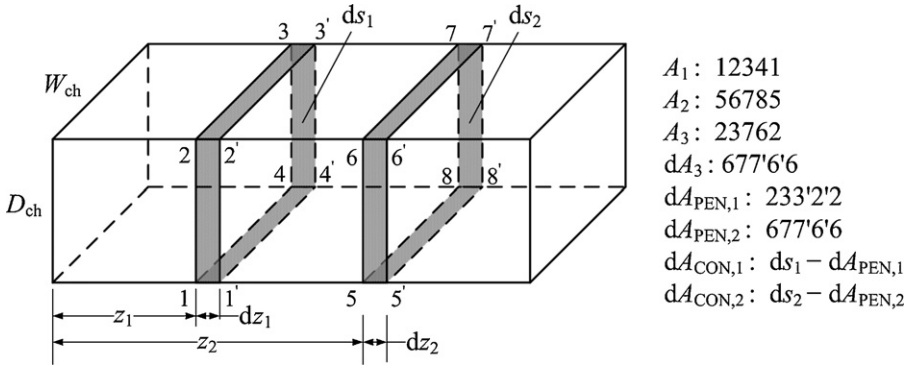

Fig. 2. Configuration for diffuse interchange in planar SOFC.

inghouse cell [1]. Fuel flows along outside of the tube, while air is first preheated via the air supply tube (AST) and then flows back into the annular area between the cathode and the air supply tube. In TSOFC, $r_{AST,in}$ and $r_{AST,out}$ are the inner and outer radius of the AST, r_{in} and r_{out} are the inner and outer radius of the cell tube. The analytical view factors between the solid phases, i.e. PEN and CON in PSOFCs, and PEN and AST in TSOFCs will be discussed in the next section.

2. Analytical differential view factors

Because the cell length (L) is generally much larger than the size in other directions, only the temperature distribution along the axial coordinate $z \in [0,L]$ is considered in our longitudinally distributed models of both planar and tubular SOFCs.

2.1. PSOFC configuration

The configuration for diffusive interchange in PSOFC is shown in Fig. 2. The view factor between two identical, parallel, and directly opposed finite rectangles ($F_{1,2}$), and the view factor between two finite rectangles of the same length, having one common edge, and 90° from each other ($F_{1,3}$), can be easily found in the view factor catalogue [11]. For the non-concave PEN surface, $dF_{dPEN1,dPEN2} = 0$. According to the reciprocity and additivity rule, the view factor between two infinitesimal elements can be directly calculated from the second-order differentiation of the finite view factors, $F_{1,2}$ and $F_{1,3}$, as shown below.

Define $X = D_{ch}/W_{ch}$, $Z = z/W_{ch}$, $Y = |Z_2 - Z_1|$,

$$dF_{dPEN1,\,dCON2} = dF_{dPEN1,\,ds2} = D_{ch}\frac{\partial^2 F_{1,3}}{\partial z_1 \partial z_2}dz_2 = -\frac{1}{\pi}f_1(X,Y)dZ_2 \quad (1)$$

$$dF_{dCON1,\,dPEN2} = \frac{dA_{PEN,2}}{dA_{CON,1}}dF_{dPEN2,\,dCON1} = -\frac{1}{\pi(1+2X)}f_1(X,Y)dZ_2 \quad (2)$$

$$dF_{dCON1,dCON2} = -\frac{W_{ch}D_{ch}}{W_{ch}+2D_{ch}}\left(\frac{\partial^2 F_{1,2}}{\partial z_1 \partial z_2} + 2\frac{\partial^2 F_{1,3}}{\partial z_1 \partial z_2}\right)dz_2 = \frac{2f_2(X,Y)}{\pi(1+2X)}dZ_2 \quad (3)$$

where

$$f_1(X,Y) = \frac{1}{2}\ln\left[\frac{Y^2(1+X^2+Y^2)}{(1+Y^2)(X^2+Y^2)}\right] - \frac{X^2}{(X^2+Y^2)^{3/2}}\tan^{-1}\left(\frac{1}{\sqrt{X^2+Y^2}}\right) \quad (4)$$

$$f_2(X,Y) = \frac{1}{2}\ln\left[\frac{(1+Y^2)(X^2+Y^2)}{(1+X^2+Y^2)Y^2}\right] + \frac{X}{(1+Y^2)^{3/2}}\tan^{-1}\left(\frac{X}{\sqrt{1+Y^2}}\right) \quad (5)$$

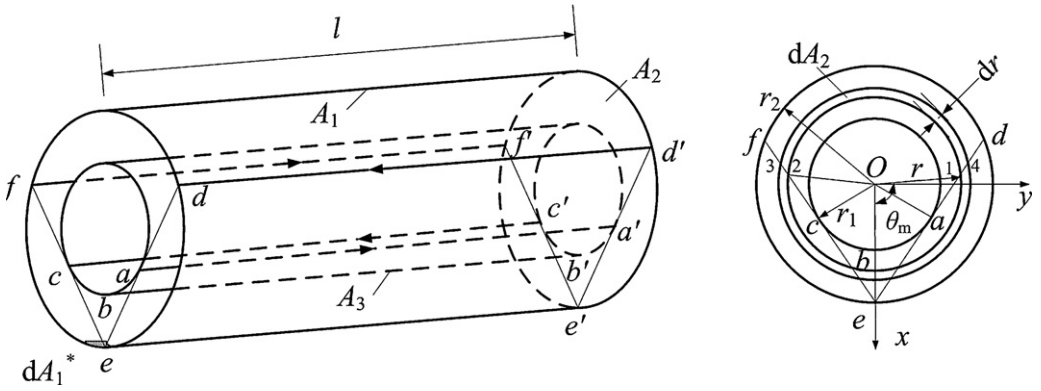

Fig. 3. Configuration for diffuse interchange in tubular SOFC.

In all expressions in which inverse trigonometric functions appear, the principal value is to be taken, i.e. for any argument x, $-\pi/2 \le \mathrm{tg}^{-1}x \le \pi/2$. The view factor from the infinitesimal element to the two opening ends of the groove ($Y_1 = z/W_{ch}$, $Y_2 = (L-z)/W_{ch}$) is related to the first-order differentiation of $F_{1,2}$ and $F_{1,3}$:

$$F_{dPEN,\,end} = \frac{D_{ch}}{W_{ch}} \frac{\partial F_{1,3}}{\partial Y}\bigg|_{Y=Y_1,Y_2} = \frac{1}{\pi} f_3(X,Y)\big|_{Y=Y_1,Y_2} \tag{6}$$

$$F_{dCON,end} = \frac{D_{ch}}{W_{ch}+2D_{ch}} \left(-\frac{\partial F_{1,2}}{\partial Y} - \frac{\partial F_{1,3}}{\partial Y}\right)\bigg|_{Y=Y_1,Y_2} = \frac{-2f_4(X,Y) - f_3(X,Y)}{\pi(1+2X)}\bigg|_{Y=Y_1,Y_2} \tag{7}$$

where

$$f_3(X,Y) = \tan^{-1}\frac{1}{Y} - \frac{Y}{\sqrt{X^2+Y^2}}\tan^{-1}\frac{1}{\sqrt{X^2+Y^2}} + \frac{Y}{2}\ln\left[\frac{Y^2(1+X^2+Y^2)}{(1+Y^2)(X^2+Y^2)}\right] \tag{8}$$

$$f_4(X,Y) = Y\ln\left[\frac{(1+Y^2)(X^2+Y^2)}{(1+X^2+Y^2)Y^2}\right] - \tan^{-1}\frac{1}{Y} - X\cdot\tan^{-1}\frac{X}{Y} + \frac{Y}{\sqrt{X^2+Y^2}}\tan^{-1}\frac{1}{\sqrt{X^2+Y^2}} + \frac{XY}{\sqrt{1+Y^2}}\tan^{-1}\frac{X}{\sqrt{1+Y^2}} \tag{9}$$

2.2. TSOFC configuration

As shown in Fig. 3, for the configuration of coaxial cylinders, the view factor $dF_{d1^*,d2}$ from the differential element ($dA_1{}^*$) at the top end of the interior surface of the outer cylinder to the differential annular element (dA_2) at the base of the outer cylinder can be calculated by the contour-integral method [12]. In the cylindrical coordinate system,

$$dF_{d1^*,\,d2} = \frac{1}{2\pi}\oint_{\frown 12+23+\frown 34+41} \frac{(y_2-y_1)dz_2 - (z_2-z_1)dy_2}{(x_2-x_1)^2+(y_2-y_1)^2+(z_2-z_1)^2} \tag{10}$$

where $x_1 = r_2$, $y_1 = 0$, $dz_2 = 0$. For the arc $\frown 12$, $x_2 = r\cos\theta$, $y_2 = r\sin\theta$, $dy_2 = r\cos\theta d\theta$, $\theta \in [\theta_m, -\theta_m]$, in which $\theta_m = \cos^{-1}(r_1/r_2) + \cos^{-1}(r_1/r)$. For the line 23, $x_2 = r\cos\theta_m$, $y_2 = -r\sin\theta_m$, $dy_2 = -r_1 r dr/r_2/(r^2-r_1^2)^{1/2}$, $r \in [r,\ r+dr]$. Line 41 is symmetric to line 23 along the x axis, and arc $\frown 34$ is in the opposite direction of arc $\frown 21$, as the radius is equal to $r+dr$.

When defining $D = r_{in}/r_{AST,out}$, $Z = z/r_{AST,out}$, $H = |Z_2 - Z_1|$, $A = (D+1)^2 + H^2$, $B = (D-1)^2 + H^2$, the view factor $F_{dPEN,end}$ between the ring element on the interior of the PEN cylinder and the annular end of channel ($z_2 = 0$, $H = Z$) is

$$F_{dPEN,\,end} = \int_{r=r_1}^{r=r_2} dF_{d1*,d2} = \frac{1}{\pi D}\left[\frac{2D^2+H^2}{\sqrt{4D^2+H^2}}\tan^{-1}\frac{\sqrt{(4D^2+H^2)(D^2-1)}}{H} - H\cdot\tan^{-1}\sqrt{\frac{D-1}{D+1}} - \frac{(A-2D)H}{\sqrt{AB}}\tan^{-1}\sqrt{\frac{A(D-1)}{B(D+1)}} - \tan^{-1}\frac{H\sqrt{D^2-1}}{H^2+2(D^2-1)}\right] \tag{11}$$

Similarly, the view factor $F_{dAST,out,end}$ between the ring element on the exterior of the AST cylinder and the annular end of the channel ($z_2 = 0$, $H = Z$) is

$$F_{dAST,\,out,\,end} = \frac{1}{\pi}\left[H\cdot\tan^{-1}\sqrt{\frac{D-1}{D+1}} + \tan^{-1}\frac{\sqrt{D^2-1}}{H} - \frac{(A-2D)H}{\sqrt{AB}}\tan^{-1}\sqrt{\frac{A(D-1)}{B(D+1)}}\right] \tag{12}$$

The view factor between $dA_1{}^*$ and the exterior surface of the inner cylinder (A_3) and the interior surface of the outer cylinder (A_1), $F_{d1^*,3}$ and $F_{d1^*,1,}$ can also be obtained by calculating the line integral along $aa'b'c'cba$ and $deff'e'd'd$, as shown in Fig. 3. The expression of $F_{d1^*,3}$ can be found in the view factor catalogue [11]. Then, the view factors between the ring elements of the PEN and the AST can be obtained by further differentiations:

$$dF_{dPEN1,\,dAST2,\,out} = \frac{\partial F_{d1*,3}}{\partial z_2}dz_2 = \frac{1}{\pi D}\left\{\left[1 - \frac{H^2(A+B)}{AB}\right]\frac{\sqrt{D^2-1}}{H^2+D^2-1} + \frac{AB(A+B)-16H^2D^2}{2(AB)^{3/2}}\tan^{-1}\sqrt{\frac{A(D-1)}{B(D+1)}} - \tan^{-1}\sqrt{\frac{D-1}{D+1}}\right\}dZ_2 \tag{13}$$

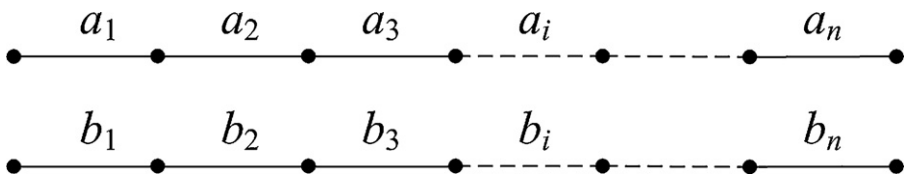

Fig. 4. Configuration of two sets of equally spaced curve segments extending along two parallel generating lines.

$$dF_{dPEN1,\,dPEN2,\,in} = \frac{\partial F_{d1*,1}}{\partial z_2} dz_2 = \frac{1}{\pi D}\left[\tan^{-1}\sqrt{D^2-1} - \frac{H(H^2+6D^2)}{(H^2+4D^2)^{3/2}}\tan^{-1}\frac{\sqrt{(H^2+4D^2)(D^2-1)}}{H} + \frac{4D^2\sqrt{D^2-1}(H^2+2D^2)}{\left(H^2+4D^2\right)\left[H^2+(H^2+4D^2)(D^2-1)\right]} - \frac{2\sqrt{D^2-1}}{H^2+4(D^2-1)}\right] dZ_2 \quad (14)$$

For the non-concave exterior surface of the AST and the PEN, $dF_{dAST1,dAST2,out} = 0$, and $dF_{dPEN1,dPEN2,out} = 0$. With the reciprocity rule, $dF_{dAST1,out,dPEN2}/dF_{dPEN1,dAST2,out} = D$.

The view factor between the ring elements on the interior surface of the AST ($dF_{dAST1,dAST2,in}$) and the view factor of the ring element to the end disk ($F_{dAST,in,end}$) can be obtained by differentiating the view factor of the disk to the parallel coaxial disk.

Define $Z = z/2/r_{AST,in}$, $X = |Z_2 - Z_1|$, then

$$dF_{dAST1,\,dAST2,\,in} = \left[1 - \frac{X(2X^2+3)}{2(X^2+1)^{3/2}}\right] dZ_2,\ F_{dAST,\,in,\,end} = \frac{2X^2+1}{2\sqrt{X^2+1}} - X \quad (15)$$

3. Analytical finite-difference view factors

The differential view factor model generally requires differential elements small enough to obtain an accurate calculation. For a typical SOFC, the cell length is usually much bigger than its characteristic size, i.e. $L \gg D_{ch}$ and $L \gg W_{ch}$ for PSOFC; and $L \gg r_{out}$ in TSOFC. So a considerable number of grids are required in distributed SOFC modeling, which leads to expensive computation. On the other hand, there are numerical discontinuities in the differential view factors of PSOFC (e.g. $f_1(X,Y) \to \infty$ as $Y = 0$ in Eq. (4)), which collapses the overall heat balance and generates unreasonable temperature distributions. The analytical finite-difference view factor is a good alternative to these problems.

Fig. 4 shows a configuration of two sets of equally spaced curve segments extending along two parallel generating lines. According to the reciprocity and additivity rules, the view factor from the continuous segments $a_i \sim a_{i+k}$ to the continuous segments $b_i \sim b_{i+k}$ can be obtained by

$$F_{a_i\sim a_{i+k},b_i\sim b_{i+k}} = \frac{1}{k+1}\left(kF_{a_i\sim a_{i+k-1},b_i\sim b_{i+k-1}} + \sum_{j=i}^{i+k-1} F_{a_{i+k},b_j}\right) + \frac{1}{k+1}\sum_{j=i}^{i+k} F_{a_j,b_{i+k}} \quad (16)$$

Because of symmetry, the view factor from the element a_i to the element b_j is only dominated by their relative positions. Define

$$F_{a_i,b_j} = F_{a_{i+k},b_{j+k}} = g\left(\left|i-j\right|\right), \quad F_{a_i\sim a_{i+k},b_i\sim b_{i+k}} = f(k+1) \quad (17)$$

and substitute it into Eq. (16) to generate:

$$(k+1)f(k+1) = kf(k) + 2\sum_{i=1}^{k} g(i) + f(1) \quad (18)$$

So,

$$g(0) = f(1), \quad g(1) = f(2) - f(1)$$
$$g(k) = \frac{1}{2}\left[(k+1)f(k+1) - 2kf(k) + (k-1)f(k-1)\right] \quad (k = 2 \ldots n-1) \quad (19)$$

3.1. PSOFC configuration

Considering a rectangular cuboids enclosed by the first k PEN elements PEN(1) ~ PEN(k) (denoted by A_1), the directly opposed CON elements CON(1) ~ CON(k) (denoted by A_2) and the two bottoms (denoted by A_3 and A_4; A_3 corresponding to the first element), the view factors $F_{1,3}(k)$ and $F_{3,4}(k)$ can be calculated using the equations for C-11 and C-14 configurations in the view factor catalogue [11]. The following equation can be generated when defining $X = D_{ch}/W_{ch}$, $\Delta l = L/n$, $Y = \Delta l/W_{ch}$:

$$f_{PEN,\,CON}(k) = 1 - 2F_{1,3}(k) \quad (k = 1 \ldots n)$$
$$f_{CON,\,CON}(k) = \frac{2(1+X)}{1+2X}\left(1 - \frac{X\left[1-F_{3,4}(k)\right]}{k(1+X)Y}\right) - \frac{2}{1+2X}\left[1-2F_{1,3}(k)\right] \quad (20)$$

The view factors $F_{PEN(i),CON(j)}$ and $F_{CON(i),CON(j)}$ in PSOFC can then be calculated by substituting Eq. (20) into Eq. (19). The view factors from the kth PEN element or CON element to the top end (top) and bottom end (bot) of the groove can be obtained by

$$F_{PEN,top}(1) = F_{1,3}(1)$$
$$F_{PEN,\,top}(k) = kF_{1,3}(k) - (k-1)F_{1,3}(k-1) \quad (k = 2 \ldots n) \quad (21)$$

$$F_{CON,\,top}(1) = \frac{X}{(1+2X)Y}\left[1-F_{3,4}(1)\right] - \frac{1}{(1+2X)}F_{1,3}(1)$$
$$F_{CON,\,top}(k) = \frac{X}{(1+2X)Y}\left[F_{3,4}(k-1) - F_{3,4}(k)\right] + \frac{1}{(1+2X)}\left[(k-1)F_{1,3}(k-1) - kF_{1,3}(k)\right] \quad (k = 2 \ldots n) \quad (22)$$

$$F_{PEN,\,bot}(k) = F_{PEN,\,top}(n+1-k)$$
$$F_{CON,\,bot}(k) = F_{CON,\,top}(n+1-k) \quad (k = 1 \ldots n) \quad (23)$$

3.2. TSOFC configuration

Considering a configuration of coaxial cylinders enclosed by the first k AST exterior elements AST, out(1) ~ AST, out(k) (denoted by A_1), the directly opposed PEN interior elements PEN, in(1) ~ PEN, in(k) (denoted by A_2) and the two annular disks

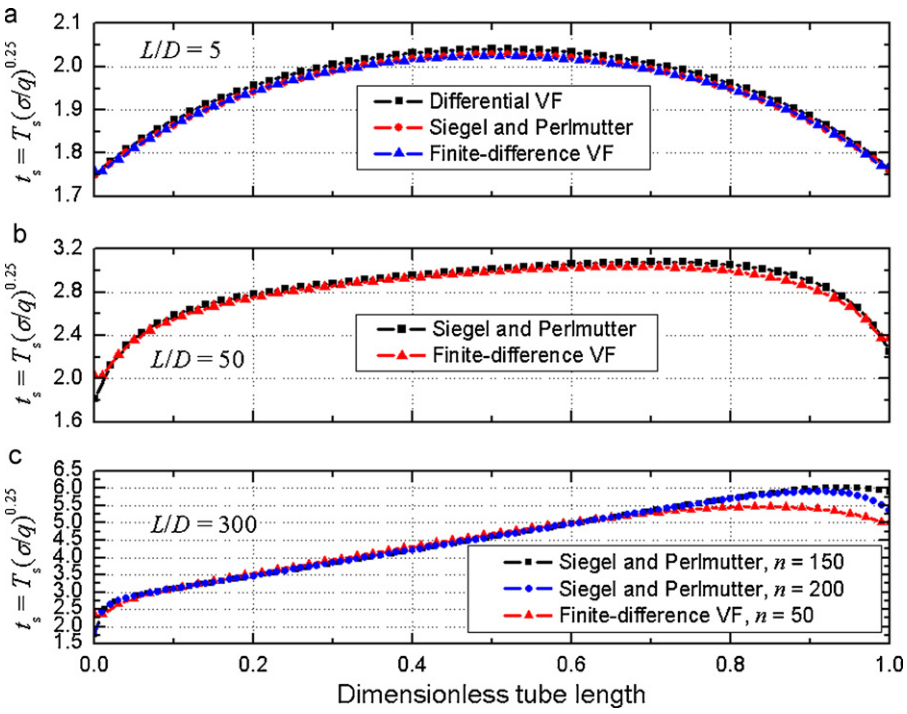

Fig. 5. Axial distribution of the dimensionless tube temperature among numerical solutions based on the differential view factor (VF) model, Siegel's and Perlmutter's method and the finite-difference view factor model at different ratio of tube length to tube diameter L/D and different grid number n.

at base or top (denoted by A_3 and A_4, and A_3 is corresponding to the first element), the view factors $F_{2,2}(k)$, $F_{2,1}(k)$, $F_{2,3}(k)$ and $F_{1,3}(k)$ can be respectively calculated using the equations for C-91, C-92, C-93 and C-77 configurations in the view factor catalogue [11]. The view factors $F_{\mathrm{PEN,in}(i),\mathrm{PEN,in}(j)}$ and $F_{\mathrm{PEN,in}(i),\mathrm{AST,out}(j)}$ in TSOFC can then be obtained by substituting $f_{\mathrm{PEN,PEN,in}}(k) = F_{2,2}(k)$ and $f_{\mathrm{PEN,AST,out}}(k) = F_{2,1}(k)$ into Eq. (19). The view factors from the kth AST exterior element or PEN interior element to the top and bottom annular ends can be calculated by

$$\begin{aligned} &F_{\mathrm{PEN,\,top}}(1) = F_{2,3}(1) \\ &F_{\mathrm{PEN,\,top}}(k) = kF_{2,3}(k) - (k-1)F_{2,3}(k-1) \quad (k = 2 \ldots n) \end{aligned} \tag{24}$$

$$\begin{aligned} &F_{\mathrm{AST,\,out,\,top}}(1) = F_{1,3}(1) \\ &F_{\mathrm{AST,\,out,\,top}}(k) = kF_{1,3}(k) - (k-1)F_{1,3}(k-1) \quad (k = 2 \ldots n) \end{aligned} \tag{25}$$

$$\begin{aligned} &F_{\mathrm{PEN,\,bot}}(k) = F_{\mathrm{PEN,\,top}}(n+1-k) \\ &F_{\mathrm{AST,\,out,\,bot}}(k) = F_{\mathrm{AST,\,out,\,top}}(n+1-k) \quad (k = 1 \ldots n) \end{aligned} \tag{26}$$

The view factor $f_{\mathrm{AST,AST,in}}(k)$ from the continuous AST interior elements AST, in(1) ~ AST, in(k) to itself can be calculated using the equation for the C-78 configuration in the view factor catalogue [11]. The view factor $F_{\mathrm{AST,in}(i),\mathrm{AST,in}(j)}$ can then be calculated by Eq. (19) and the view factor from the kth AST interior element to the circular end can be obtained by

$$\begin{aligned} &F_{\mathrm{AST,\,in,\,end}}(1) = 0.5\left[1 - f_{\mathrm{AST,\,AST,\,in}}(1)\right] \\ &F_{\mathrm{AST,\,in,\,end}}(k) = 0.5\left[1 - kf_{\mathrm{AST,\,AST,\,in}}(k) + (k-1)f_{\mathrm{AST,\,AST,\,in}}(k-1)\right] \\ &(k = 2 \ldots n) \end{aligned} \tag{27}$$

4. Simulation and discussions

4.1. Problem of convective and radiant heat transfer

For problems of convective and radiant heat transfer for flow of a transparent gas in a tube with a gray wall, the governing equations for the gas and solid phases are, respectively [12,13]:

$$\rho_g u_g c_{p,g} \frac{dT_g}{dz} = \frac{4}{D} h(T_s - T_g),\ T_g|_{z=0} = T_{g,\mathrm{in}} \tag{28}$$

$$0 = -\frac{\varepsilon}{1-\varepsilon}\left(\sigma T_s^4 - B_s\right) + h(T_g - T_s) + q \tag{29}$$

where z is the axial length coordinate measured from the tube entrance, T_g is the gas temperature, $T_{g,in}$ is the inlet gas temperature, ρ_g is the gas density, u_g is the mean gas velocity, $c_{p,g}$ is the mass specific heat of gas, h is the convective heat-transfer coefficient, D is the tube diameter, T_s is the tube temperature, $\sigma = 5.67 \times 10^{-8}\,\mathrm{W\,m^{-2}\,K^{-4}}$ is the Stefan–Boltzmann constant, ε is the emissivity of solid phase, q is the heat added per unit area at the tube wall. Note that the conductive heat transfer is not included in Eq. (29). The total outgoing radiation per unit area from a tube surface element B_s is related to the tube temperature and view factors:

$$B_s(z) = \varepsilon\sigma T_s^4 + (1-\varepsilon)\left[\int_0^L B_s(\xi)\mathrm{d}F_{z,\xi} + \sigma T_{e,\mathrm{in}}^4 F_{z,\mathrm{in}} + \sigma T_{e,\mathrm{out}}^4 F_{z,\mathrm{out}}\right] \tag{30}$$

where $\mathrm{d}F_{z,\xi} = K(|z-\xi|)\mathrm{d}\xi$ is the differential view factor between two ring elements at location z and ξ, $K(|z-\xi|)$ is the geometric kernel, $F_{z,in}$ and $F_{z,out}$ are the view factors from an element at location z to the circular opening at the inlet and outlet ends of the tube, respectively. For a circular tube, $K(|z-\xi|)$, $F_{z,in}$ and $F_{z,out}$ can be calculated using Eq. (15). $T_{e,in}$ and $T_{e,out}$ are the effective black-body temperature of the environment at the inlet and outlet end openings, which are usually set to be the inlet and outlet gas temperatures, i.e. $T_{e,in} = T_{g,in}$, $T_{e,in} = T_{g,out} = T_g|_{z=L}$ [13].

An additional check for each numerical solution can be made by making sure that it always satisfies an overall heat balance. The total input heat to the tube wall Q_{in} is

$$Q_{\mathrm{in}} = \pi D\left(qL + \int_0^L \sigma T_{e,\mathrm{in}}^4 F_{z,\mathrm{in}}\,dz + \int_0^L \sigma T_{e,\mathrm{out}}^4 F_{z,\mathrm{out}}\,dz\right) \tag{31}$$

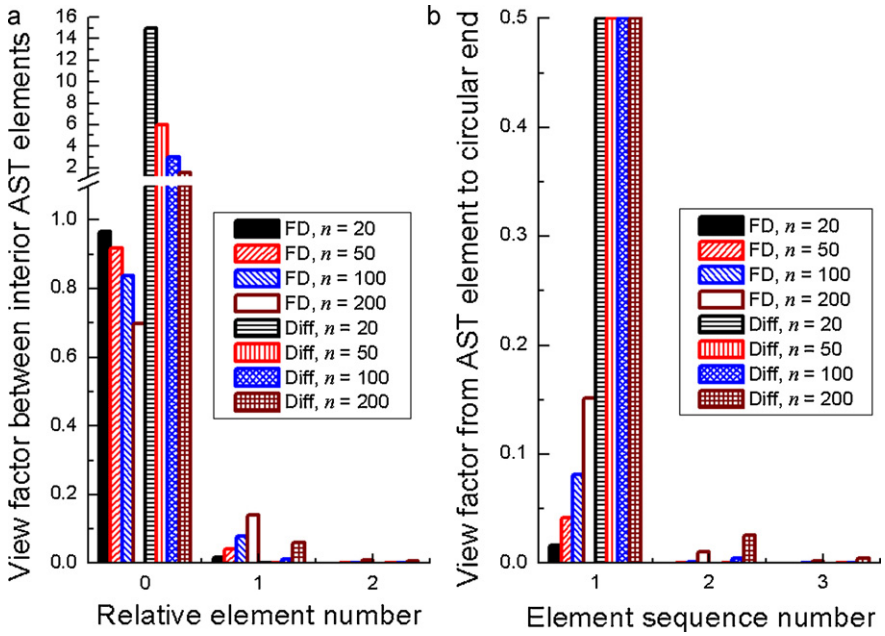

Fig. 6. Comparison between the finite-difference (FD) and first-order approximation of differential (Diff) view factors (a) between interior tube ring elements (b) from an interior tube ring element to the circular end at different grid number n. The relative element number equal to zero means two directly opposed elements and the element sequence number equal to 1 represents the first element adjacent to the inlet opening end.

and the total output heat from the tube wall Q_{out} is

$$Q_{out} = \tfrac{1}{4}\pi D^2 \rho_g u_g c_{p,g}(T_{g,out} - T_{g,in}) + \pi D\left(\int_0^L B_s(z)F_{z,in}\,dz + \int_0^L B_s(z)F_{z,out}\,dz\right) \quad (32)$$

The overall heat balance is satisfied when $Q_{in} = Q_{out}$; the relative error on the overall heat balance is then defined as $|1 - Q_{out}/Q_{in}|$.

When defining the dimensionless coordinate as $Z = z/D$, Stanton number as $S = 4h/(\rho_g u_g c_{p,g})$, dimensionless temperature as $t = T(\sigma/q)^{1/4}$ and the dimensionless heat-transfer coefficient as $H = (h/q)(q/\sigma)^{1/4}$, Eqs. (28)–(32) can be reduced to dimensionless form [13]. Siegel and Perlmutter further transformed the integral equation (30) to a second-order differential equation by use of an approximate exponential function for the geometric kernel K [13]. However, it requires complex mathematical derivations to find the two boundary conditions. When the conductive heat transfer is considered in Eq. (29), it will generate a fourth-order equation.

Fig. 5 shows the axial distribution of the dimensionless tube temperature for three different numerical solutions. The first solution is from the dimensionless form of Eqs. (28)–(30) with the differential view factors in Eq. (15), the second solution is from the second-order differential system of Siegel and Perlmutter, and the third solution is obtained from manual discretization of Eqs. (28)–(30) with the finite-difference view factors in Eqs. (19) and (27). With the following parameters $\varepsilon = 0.8$, $q = 1 \times 10^4\ \mathrm{W\,m^{-2}}$, $S = 0.00988$, $H = 0.8$, $t_{g,in} = 1.5$, all three numerical solutions were calculated using the commercial software gPROMS, which provides equation-based solvers for differential and integral hybrid systems [14]. As shown in Fig. 5(a), for a short tube with $L/D = 5$, all three numerical methods led to an identical temperature distributions at a default grid number $n = 50$, and the relative errors on the overall heat balance were 0.0245, 5.24×10^{-4} and 5.55×10^{-16} for the differential view factors solution, Siegel and Perlmutter solution, and finite-difference view factors solution, respectively. When $L/D = 50$ and $n = 50$, the element size is comparable to the tube diameter $dz = L/n = D$, but it then becomes difficult to obtain a solution that converges when using the differential view factors method. As shown in Fig. 5(b), the temperature distribution based on finite-difference view factors is smoother than that obtained using Siegel's and Perlmutter's computation, while the relative error on the overall heat balance 2.49×10^{-13} is much smaller than that for the Siegel's and Perlmutter method (0.00169). In the commercial Westinghouse TSOFC design, the size of the air supply tube is $r_{AST,in} = 2.5 \times 10^{-3}$ m and its length is $L = 1.5$ m, which means a high L/D ratio of 300. In this case, a numerical convergence using Siegel's and Perlmutter's method also requires a large grid number to get a small element size. When $n = 150$ and $n = 200$, the relative errors on the overall heat balance using the Siegel's and Perlmutter's method are up to 0.538 and 0.164, respectively. As shown in Fig. 5(c), the computation based on the finite-difference view factors displays a different temperature distribution for the second half of tube. It took only 30 ms for the computation based on the finite-difference view factor model to find a solution with a very small relative error on the overall heat balance 1.177×10^{-14} by keeping a default grid number $n = 50$ at $L/D = 300$.

The above problem can be further explained when comparing the finite-difference and differential view factors methods. According to the physical meaning of the view factors, their value should be not greater than unity. As shown in Fig. 6(a), the finite-difference view factors between the interior AST elements always follow this rule, while the differential view factors appear to be always greater than 1 for the two directly opposed elements even for $n = 200$. Here, the differential view factors are calculated by approximation of the first-order differences, i.e. $dF_{z,\xi} = K(|z - \xi|)d\xi \approx KL/n$. For large value of L/D and small grid number n, the element size is comparable to the characteristic size ($dz = L/n \approx D$), which leads to computational problem with differential view factors. As shown in Fig. 6(b), the view factor from the first infinitesimal interior AST element to the circular end is equal to 0.5, independently of the grid numbers ($F_{dAST,in,end} = 0.5$ as $X = 0$ in Eq. (15)), and the corresponding finite-difference view factors are much lower than this limiting value ($F_{AST,in,end}(1) = 0.5$ as $n \to \infty$). Fig. 7 shows similar results for the differential and finite-difference view factors for TSOFC with $r_{AST,out} = 4 \times 10^{-3}$ m, $r_{in} = 8.66 \times 10^{-3}$ m and $L = 1.5$ m.

Numerical problems are more pronounced in the computation of radiation heat transfer in planar SOFCs, because of discontinu-

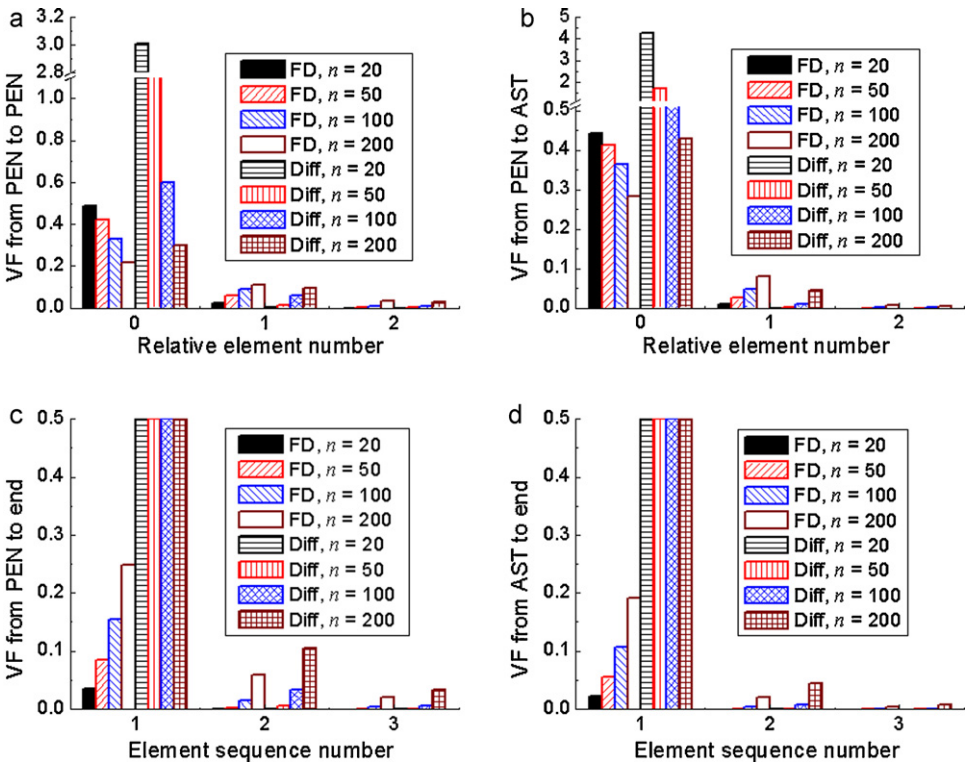

Fig. 7. Comparison between the finite-difference (FD) and first-order approximation of differential (Diff) view factors (VF) (a) from PEN element to PEN element, (b) from PEN element to AST element, (c) from PEN element to the annular end and (d) from AST element to the annular end in the tubular SOFC configuration. The relative element number equal to zero means two directly opposed elements and the element sequence number equal to 1 represents the first element adjacent to the inlet opening end.

ities in the geometric kernel when considering differential view factors. With a typical PSOFC geometry [15], $W_{ch} = 3 \times 10^{-3}$ m, $D_{ch} = 1 \times 10^{-3}$ m, $L = 0.1$ m, Fig. 8 shows a comparison between the finite-difference view factors and the first-order approximation of the differential view factors in the PSOFC configuration. As shown in Fig. 8(a) and (b), the finite-difference view factors between PEN and CON elements are always lower than unity, while the differential view factors between two directly opposed elements are infinite

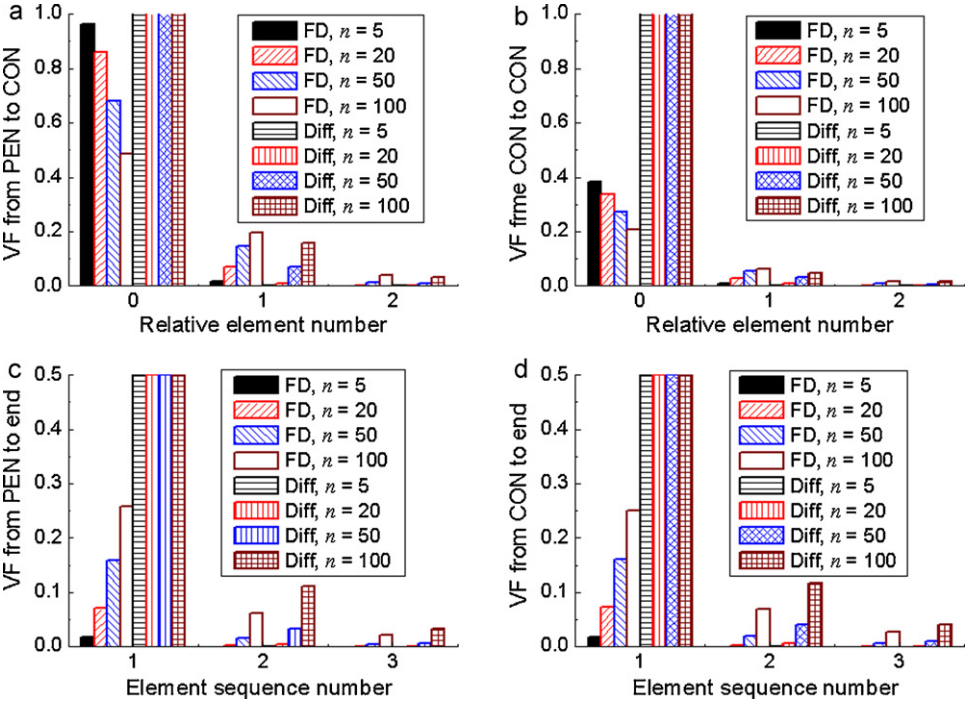

Fig. 8. Comparison between the finite-difference (FD) and first-order approximation of differential (Diff) view factors (VF) (a) from PEN element to CON element, (b) from CON element to CON element, (c) from PEN element to end and (d) from CON element to end in the planar SOFC configuration. The relative element number equal to zero means two directly opposed elements and the element sequence number equal to 1 represents the first element adjacent to the inlet opening end.

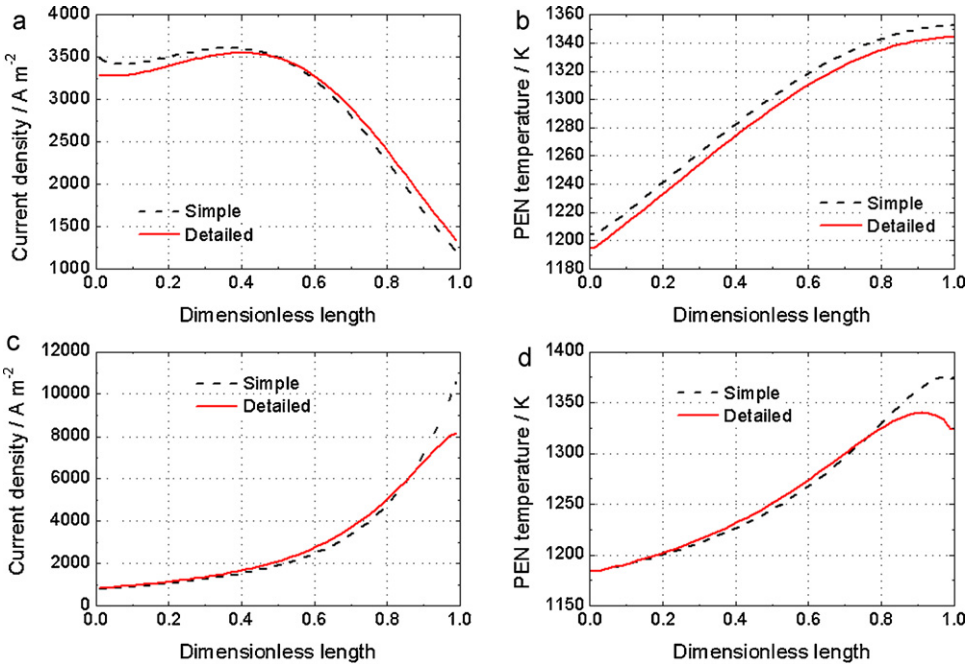

Fig. 9. Distribution of the current density and solid temperature from the distributed cell model with interface (INT-) type PEN model (assuming that electrochemical reactions only occur at the electrode/electrolyte interface, and reforming and water gas shift chemical reactions only occur at the anode/flow channel interface) for 90% H_2–10% H_2O fuel system. (a) and (b) under co-flow condition, (c) and (d) under counter-flow condition. The geometries of PSOFC are: cathode thickness $\delta_a = \delta_c = 50\ \mu m$, electrolyte thickness $\delta_e = 150\ \mu m$, channel width $W_{ch} = 3$ mm, channel depth $D_{ch,a} = D_{ch,c} = 1$ mm, rib width $W_{rib} = 2.42$ mm, total bipolar plate depth $D_{t,a} = D_{t,c} = 2.5$ mm, channel length $L = 100$ mm, and the number of channels $n_{ch} = 18$ [15].

($f_1(X,Y) \to \infty$ and $f_2(X,Y) \to \infty$ as $Y = 0$ in Eqs. (4) and (5)). As shown in Fig. 8(c) and (d), the view factor from the first infinitesimal PEN and CON elements to the opening end is equal to 0.5 at different grid numbers ($F_{dPEN,end} = 0.5$ and $F_{dCON,end} = 0.5$ as $Y = 0$ in Eqs. (6) and (7)), and the corresponding finite-difference view factors are much lower than this limiting value ($F_{PEN,end}(1) = 0.5$ and $F_{CON,end}(1) = 0.5$ as $n \to \infty$).

4.2. Application to distributed SOFC model

The energy conversation in the PEN is [10]:

$$\rho_{PEN} c_{p,PEN} \frac{\partial T_{PEN}}{\partial t} = \kappa_{PEN} \frac{\partial^2 T_{PEN}}{\partial z^2} - S_{m,PEN,c} \sum_i N_{i,c}|_{C/C} H_{c,i}(T_c) + \frac{S_{m,PEN,a}}{2} \sum_i \left[\left(N_{i,a}\big|_{A/C} + \left| N_{i,a}\big|_{A/C} \right| \right) H_{a,i}(T_a) + \left(N_{i,a}\big|_{A/C} - \left| N_{i,a}\big|_{A/C} \right| \right) H_{a,i}(T_{PEN}) \right] - S_{m,PEN,c} I(z) V_{cell} + \sum_{k=a,c} S_{h,PEN,k} h_{k,PEN}(T_k - T_{PEN}) - \sum_{k=a,c} S_{h,PEN,k} q_{PEN,k} \quad (33)$$

where ρ_{PEN}, $c_{p,PEN}$, κ_{PEN} are the density, mass specific heat capacity, and heat conductivity of the PEN; $S_{m,PEN,k}$ and $S_{h,PEN,k}$ are the effective mass and heat transfer area per unit volume of PEN between gas and solid phases in the anode ($k = a$) and cathode ($k = c$) flow channels; T_a, T_c, T_{PEN} are the temperatures of fuel, air and PEN, h is the corresponding convective heat transfer coefficient, H_i is the molar specific enthalpy of species i, N_i is the molar flux of species i at the electrode/flow channel interface (anode side: A/C; cathode side: C/C), $I(z)$ is the local current density, and V_{cell} is the cell voltage which is assumed uniformly distributed along the z coordinate.

On the right hand side of Eq. (33), the first item is heat conduction, summations of the second and third items are the total electrochemical and chemical reaction heats, the fourth item is the electric power, the fifth item is the convective heat transfer between the gas phase and the PEN, and the sixth item is the radiation heat transfer. For gray bodies, the radiation heat flux out of the PEN element surface, q_{PEN} is obtained by

$$q_{PEN,k}(z) = \frac{\varepsilon_{PEN} \left[\sigma T_{PEN}^4(z) - B_{PEN}(z) \right]}{1 - \varepsilon_{PEN}} \quad (k = a,\ c) \quad (34)$$

For PSOFC configuration,

$$B_{PEN,k}(z) = \varepsilon_{PEN} \sigma T_{PEN}^4(z) + (1 - \in_{PEN}) \sigma T_e^4 F_{dPENz,end,k} + (1 - \varepsilon_{PEN}) \left[\int_0^L B_{PEN}(x) dF_{dPENz,dPENx,k} + \int_0^L B_{CON,k}(x) dF_{dPENz,dCONx,k} \right] \quad (35)$$

$$B_{CON,k}(z) = \varepsilon_{CON} \sigma T_{CON}^4(z) + (1 - \varepsilon_{CON}) \left[\sigma T_e^4 F_{dCONz,end,k} + \int_0^L B_{CON,k}(x) dF_{dCONz,dCONx,k} + \int_0^L B_{PEN,k}(x) dF_{dCONz,dPENx,k} \right] \quad (36)$$

where ε_{PEN} and ε_{CON} are the emissivities of PEN and CON, B_{PEN} and B_{CON} are the total outgoing radiation per unit area from the PEN and CON element surfaces, respectively, and T_e is the effective black-body temperature of the environment, which is set to be the gas temperature at the corresponding end of the flow channel [13]. Note that the analytical differential view factors are used here, which should be replaced by the analytical finite-difference view factors when using the discrete governing equations. The energy balances for the CON in PSOFC and AST in TSOFC are simpler and can be obtained similarly [10].

In contrast to the detailed radiation model mentioned above, only surface-to-surface radiation exchange between two directly

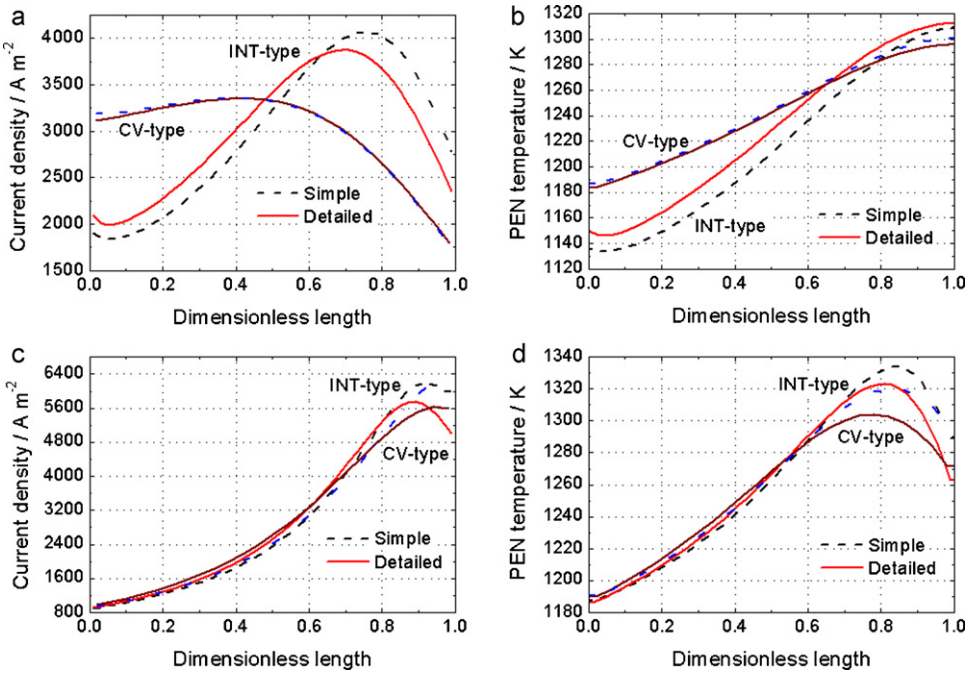

Fig. 10. Distribution of the current density and solid temperature from the distributed cell model with INT-type PEN model and control volume (CV-) type PEN model (electrochemical and chemical reactions occur everywhere in electrodes) for 30% pre-reformed methane-fueled system. (a) and (b) under co-flow condition, (c) and (d) under counter-flow condition. The geometries of PSOFC are the same as those in Fig. 9.

opposed elements is taken into account in most of the state-of-the-art SOFC models [4–6]. For an assumed enclosed system of PEN-CON rectangle, the simple radiation model means

$$q_{\mathrm{PEN},k} = \frac{\sigma\left(T_{\mathrm{PEN}}^4 - T_{\mathrm{CON}}^4\right)}{1/\varepsilon_{\mathrm{PEN}} + W_{\mathrm{ch}}(1/\varepsilon_{\mathrm{CON}} - 1)/(W_{\mathrm{ch}} + 2D_{\mathrm{ch},k})} \quad (k = \mathrm{a},\ \mathrm{c}) \tag{37}$$

Our SOFC model was validated by comparison with experimental data from the IEA Benchmark Test for a typical PSOFC design [15]. For both H_2–H_2O and pre-reformed methane fuel systems, the operating pressure is 1 bar, the air and fuel inlet temperatures are 900 °C, the air stoichiometry is 7, and the overall fuel utilization is 85%. When the analytical differential view factors are used, the built-in discrete methods of gPROMS fail to obtain a solution with a satisfactory relative error on the overall heat balance because of the discontinuity problem in the PSOFC configuration. Based on the analytical model of finite-difference view factors and stagger grids, a fast (average 10 s for 50 discrete grids) and accurate solution is obtained with a relative error of the overall heat balance <0.1% [10].

Fig. 9 shows the distribution of the current density and PEN temperatures under both co-flow and counter-flow conditions for 90%H_2–10%H_2O fuel system. Under the co-flow condition, as shown in Fig. 9(b), the solid temperature predicted based on the "detailed" radiation model is almost 10 K lower than the "simple" calculation. More importantly, the smaller solid temperature gradient implies a smaller thermal stress from the "detailed" prediction than from the "simple" prediction. Under the counter-flow condition, as shown in Fig. 9(d), there is an obvious nonlinear distribution of the PEN temperature in the "detailed" calculation, which is not well captured in the "simple" calculation. Because of the strong radiant heat loss to the environment in the "detailed" calculation, the maximum negative gradient of the solid temperature appears close to the fuel inlet. Compared to the "simple" calculation, the "detailed" calculation avoids the overestimation of the maximum current density and solid temperature (especially under counter-flow condition), which provides a more uniform distribution of the current density as shown in Fig. 9(a) and (c).

Fig. 10 shows the distribution of the current density and solid temperature under co-flow and counter-flow conditions for fuel system of 17.1%CH_4–26.26H_2–49.34%H_2O–2.94%CO–4.36% CO_2, which means 30% pre-reformed gas at CO shift equilibrium resulting from a methane/water mixture with a molar ratio of H_2O/CH4 = 2.5. Similar to the results with the H_2–H_2O fuel system, the distributions of the current density and solid temperature from the "detailed" calculation are more uniform than those from the "simple" calculation. The maximum PEN temperature and cell performance in the "detailed" calculation are also generally lower than in the "simple" calculation. Unlike the results in Fig. 10(b) and (d) shows a non-monotonic distribution of PEN temperature in both the "simple" and "detailed" calculation under counter-flow conditions because of the strongly endothermic methane reforming reaction. By considering the radiant heat loss to the environment, the "detailed" radiant model led to a more intense negative gradient in solid temperature close to the fuel inlet. As a result, Fig. 10(c) shows a nonlinear distribution of the current density in the "detailed" calculation.

5. Conclusions

Radiation heat transfer plays an important role in temperature distribution in solid oxide fuel cells (SOFC). A SOFC model with a detailed radiation model is necessary for accurately predicting the cell performance. For the two typical designs of tubular and planar configurations, a mathematical model of view factors for radiation heat exchange in longitudinally distributed SOFC modeling was introduced in this paper.

An analytical model of differential view factors was first developed for the configurations of diffusive interchange in planar and tubular SOFCs. An accurate solution is usually obtainable when the size of the differential elements is small enough. However, the cell length is generally much larger than its characteristic size in

a typical SOFC. So a large amount of discrete grids are required to ensure numerical accuracy, which leads to expensive computation. In the case of planar configuration, the differential view factor model failed because of the discontinuities of some geometric kernels. An analytical model of finite-difference view factors was then developed to resolve the non-convergence problem of the solution.

The mathematical model of view factors was first validated via comparison of known results of a classical problem of convective and radiant heat transfer in the case of flow of a transparent gas in a tube with a gray wall. All computational results were compared to Siegel's and Perlmutter's solution by transforming the integral equation of radiant energy balance into a second-order differential equation [13]. For a small ratio of tube length to tube diameter (L/D), the differential view factor model leads to an accurate solution. For a large L/D ratio, numerical convergence using Siegel's and Perlmutter's method requires a large grid number to get a small element size. A fast and accurate computation is available for the finite-difference view factor model with a very small relative error for the overall heat balance by keeping a default grid number ($n = 50$) without a limitation of large L/D ratio. Another advantage of the finite-difference view factor model is that it avoids extra complex mathematical derivations of the governing equations like the ones Siegel and Perlmutter did.

In addition to a simple radiation model, a detailed radiation model based on the analytical view factors was then applied to an in-house distributed cell model and solved using the commercial software gPROMS for a typical PSOFC configuration [10]. Compared to the simple radiation model, which only takes into account the surface-to-surface radiation exchange between two directly opposed elements, the distributed cell model with the detailed radiation model predicts more uniform distributions of the local current density and solid temperature, which also means a smaller thermal stress. In principle, the analytical view factors models can be applied to other types of cell designs with regular geometry, such as the flattened tubular SOFC and integrated planar SOFC.

Acknowledgement

Financial support from Natural Science Foundation (grant No. 50706019) is gratefully acknowledged.

References

[1] J.F. Hirschenhofer, D.B. Stauffer, R.R. Engleman, Fuel Cell Hand Book, 7th ed., U.S. Department of Energy, Morgantown, 2004.
[2] F.J. Gardner, M.J. Day, M.P. Brandon, M.N. Pashley, M. Cassidy, J. Power Sources 86 (2000) 122–129.
[3] D.L. Damm, A.G. Fedorov, J. Fuel Cell Sci. Technol. 2 (2005) 258–262.
[4] S. Nagata, A. Momma, T. Kato, Y. Kasuga, J. Power Sources 101 (2001) 60–71.
[5] P. Aguiar, C.S. Adjiman, N.P. Brandon, J. Power Sources 138 (2004) 120–136.
[6] T.W. Song, J.L. Sohn, J.H. Kim, T.S. Kim, S.T. Ro, K. Suzuki, J. Power Sources 142 (2005) 30–42.
[7] R.J. Braun, Optimal Design and Operation of Solid Oxide Fuel Cell Systems DS Dissertation, University of Wisconsin-Madison, Madison, 2002.
[8] C. Stiller, B. Thorud, S. Seljebo, O. Mathisen, H. Karoliussen, O. Bolland, J. Power Sources 141 (2005) 227–240.
[9] C. Bao, Y.X. Shi, C. Li, N.S. Cai, Q.Q. Su, Int. J. Hydrogen Energy 35 (2010) 2894–2899.
[10] C. Bao, Y.X. Shi, E. Croiset, C. Li, N.S. Cai, J. Power Sources 195 (2010) 4871–4892.
[11] http://www.me.utexas.edu/~howell/index.html.
[12] E.M. Sparrow, R.D. Cess (Eds.), Radiation Heat Transfer Rev., Wadsworth, Belmont, CA, 1977.
[13] R. Siegel, M. Perlmutter, Int. J. Heat Mass Transfer 5 (1962) 639–660.
[14] Process Systems Enterprise Ltd. gPROMS Advanced User Guide. London, 2004.
[15] E. Achenbach, International Energy Agency. Annex II, Modelling and evaluation of advanced SOFC, Subtask A: Numerical modelling, Experimental Data Base and Validation, Activity A2: Stack Modeling, 1995.